

Full length article

Macroscopic to nanoscopic *in situ* investigation on yielding mechanisms in ultrafine grained medium Mn steels: Role of the austenite-ferrite interface

Binhan Sun ^{a,*}, Yan Ma ^b, Nicolas Vanderesse ^c, Rama Srinivas Varanasi ^a, Wenwen Song ^b, Philippe Bocher ^c, Dirk Ponge ^{a,**}, Dierk Raabe ^a

^a Max-Planck-Institut für Eisenforschung GmbH, Max-Planck-Straße 1, 40237, Düsseldorf, Germany

^b Steel Institute, RWTH Aachen University, Intzestraße 1, 52072, Aachen, Germany

^c Department of Mechanical Engineering, École de Technologie Supérieure, 1100 Notre-Dame Ouest Street, Montreal, QC, H3C 1K3, Canada

ARTICLE INFO

Article history:

Received 23 April 2019

Received in revised form

13 July 2019

Accepted 24 July 2019

Available online 30 July 2019

Keywords:

Medium Mn steels

Discontinuous yielding

Lüders band

Austenite-ferrite interface

Dislocation generation

ABSTRACT

Ultrafine austenite-ferrite duplex medium Mn steels often show a discontinuous yielding phenomenon, which is not commonly observed in other composite-like multiphase materials. The underlying dislocation-based mechanisms are not understood. Here we show that medium Mn steels with an austenite matrix (austenite fraction ~65 vol%) can exhibit pronounced discontinuous yielding. A combination of multiple *in situ* characterization techniques from macroscopic (a few millimeters) down to nanoscopic scale (below 100 nm) is utilized to investigate this phenomenon. We observe that both austenite and ferrite are plastically deformed before the macroscopic yield point. In this microplastic regime, plastic deformation starts in the austenite phase before ferrite yields. The austenite-ferrite interfaces act as preferable nucleation sites for new partial dislocations in austenite and for full dislocations in ferrite. The large total interface area, caused by the submicron grain size, can provide a high density of dislocation sources and lead to a rapid increase of mobile dislocations, which is believed to be the major reason accounting for discontinuous yielding in such steels. We simultaneously study the Lüders banding behavior and the local deformation-induced martensite forming inside the Lüders bands. We find that grain size and the austenite stability against deformation-driven martensite formation are two important microstructural factors controlling the Lüders band characteristics in terms of the number of band nucleation sites and their propagation velocity. These factors thus govern the early yielding stages of medium Mn steels, due to their crucial influence on mobile dislocation generations and local work hardening.

© 2019 Acta Materialia Inc. Published by Elsevier Ltd. All rights reserved.

1. Introduction

Medium Mn steels (3–12 wt% Mn) emerge as strong candidate alloys for the 3rd generation of advanced high strength steels, due to their excellent strength-ductility combination (product of tensile strength and total elongation up to ~70 GPa% [1]), simple heat treatment process (e.g. intercritical annealing (IA)), and low-cost alloy ingredients. The composite-like microstructure (normally ferrite and metastable austenite) combined with submicron grain

scale [1–3] differentiates such materials from other types of alloys. Yet, a drawback of these steels is that they often show a discontinuous yielding phenomenon [2–9]. This is characterized by a yield point drop followed by a stress plateau (also referred to as yield point elongation, YPE) in the tensile stress-strain curves and the formation of Lüders bands. Such localized deformation phenomena could deteriorate the surface quality during forming operations. From a fundamental viewpoint, it is interesting to study this effect in more detail, since discontinuous yielding has rarely been observed in other multiphase composite-like alloys (e.g. conventional transformation-induced plasticity (TRIP) [10], dual phase [11] and duplex stainless steels [12]).

Previous studies on this phenomenon have mainly probed variations in processing parameters with respect to the appearance of

* Corresponding author.

** Corresponding author.

E-mail addresses: b.sun@mpie.de (B. Sun), d.ponge@mpie.de (D. Ponge).

discontinuous yielding and the YPE value (approximately equals the Lüders strain) [2–5,7]. A few investigations focus on the characteristics of Lüders band nucleation and propagation [9,13]. He et al. [14] studied the initiation of plasticity in different phases by nanoindentation. Despite solid experimental results reported in the previous literature, no clear picture of the underlying mechanisms of discontinuous yielding has emerged. The main observations and open questions regarding this phenomenon in medium Mn austenite–ferrite steels can be summarized as follows:

- (a) The YPE value acquired from room-temperature tensile testing at quasi-static strain rates substantially decreases with higher IA temperature [3,4,6,8]. After exposing the material to a critical IA temperature, discontinuous yielding changes into a continuous flow pattern ($YPE = 0$) [6]. Since changes in the IA treatment affect many microstructural parameters at the same time including phase fraction and stability, partitioning and composition, size, phase morphology and percolation, and dislocation density [1,5–7], it is difficult to deduce critical factors governing discontinuous yielding in such steels.
- (b) A laminated ferrite plus austenite microstructural morphology produced by IA from an initially quenched martensitic structure can effectively suppress discontinuous yielding [2,5,7]. Han et al. [2] attributed this to the co-deformation of austenite and ferrite, whereas Steineder et al. [7] proposed the enhanced work hardening capacity of the laminated phases as the reason.
- (c) A few studies on some medium Mn steels with discontinuous yielding suggested that ferrite starts to yield at a lower stress level compared to austenite [2,14]. However, other investigations showed that austenite was softer than ferrite [15], yet, these materials also exhibited discontinuous yielding.

This brief list shows that some observations and explanations are not consistent and in part even contradictory, revealing lack of elementary dislocation-based understanding of discontinuous yielding in medium Mn steels.

For single phase materials the locking-unlocking theory has been used to explain discontinuous yielding [16,17]. It suggests that solutes segregate to grown-in defects and lock them. Such interaction can occur between interstitial atoms (e.g. C and N) and dislocation core regions in body-centered cubic (BCC) metals, a mechanism referred to as Cottrell–Bilby effect [16]. In face-centered cubic (FCC) materials with low stacking fault energy, interstitial solutes interact only weakly with dislocations. Yet, some substitutional (e.g. Mn) solutes segregate to stacking faults as proposed by Suzuki [18]. The stress needed to unlock these defects from the solute atmosphere is higher than the stress to move them. This depinning effect thus causes abrupt and rapid plastic flow avalanches, resulting in a yield drop and the nucleation of localized deformation (i.e. Lüders) bands. Although solute locking of dislocations in terms of the Cottrell theory has been revealed in part even by near-atomic scale probing [19–21], the associated dominant role of dislocation unlocking on the abrupt yield drop was questioned by several studies [19,22]. An alternative mechanism based on dislocation multiplication was thus suggested based on the model of Johnston and Gilman [19,22,23]. The model proposes three factors that promote discontinuous yielding: an initially low density of mobile dislocations, rapid dislocation multiplication upon loading and a relatively low sensitivity of dislocation velocity to applied stress [19,22]. In this model, the stress ceases to increase (thus marking the upper yield point) when the plastic strain rate of the specimen that increases with the density and velocity of mobile

dislocations equals the applied strain rate (crosshead speed divided by the gage length).

Most medium Mn steels investigated so far have a ferritic matrix (ferrite fraction above 50 vol%), which encouraged most researchers to interpret discontinuous yielding in terms of the Cottrell–Bilby mechanism [2–4,14]. In the present study, we show that a medium Mn steel with austenite matrix (austenite fraction ~65 vol%) can also exhibit pronounced discontinuous yielding. In order to reveal the underlying mechanisms, dynamic observation of the microstructural evolution during micro- and macro-yielding at high spatial resolution and good probing statistics are required. We address this challenge by combining multiple *in situ* microstructural characterization techniques from macroscopic (a few mm) down to nanoscopic scale (below 100 nm). The results enable us to discuss the origin of discontinuous yielding in medium Mn steels. In addition, it has been shown that the Lüders band formation and propagation in medium Mn steels are accompanied with localized deformation-induced austenite to martensite transformation [6,13,24,25]. This phenomenon has rarely been reported in other types of steels. However, the influence of stress- or strain-induced martensite formation on the yielding and Lüders banding behavior is not clearly revealed in the previous reports, which could be due to two factors. Firstly, the effect of deformation-induced martensite has not been decoupled from many other varying factors including phase fraction, composition, size, morphology and initial dislocation density [3,6,8]. Except the mechanical stability of austenite which directly controls the kinetics of deformation-induced martensite formation, other microstructural variates should be maintained to be minimum. Secondly, a dynamic and simultaneous characterization of the Lüders banding behavior and local martensite formation on the same specimen has not yet been applied. In the present study, we design our experiments in a way that we modify the microstructure only in terms of two parameters, namely, grain size and austenite stability. A novel *in situ* probing method consisting of correlative digital image correlation (DIC) and magnetic induction measurement has been developed and utilized to probe the local strain and local deformation-induced martensite at the same time and at the same specimen positions. This approach provides a more detailed access to the role of deformation-induced martensite on the Lüders banding behavior in such steels.

2. Experimental procedure

2.1. Materials and processing

The chemical composition of the investigated steel is 0.2C–10.2Mn–2.8Al–1Si (in wt.%). The steel was designed for a large fraction of austenite (above 50 vol%) upon suitable heat treatments. Casting and hot rolling schedules have been described elsewhere [15]. The hot rolled material was then heat treated at 700 °C for 2 h, followed by cold rolling to a total thickness reduction of ~50%. The cold rolled steel possesses a predominately ferritic microstructure (ferrite and martensite) and a small amount of retained austenite (~20%). Inter-critical annealing was adopted to produce an ultrafine austenite–ferrite microstructure. The cold rolled steel was annealed in a box furnace at 800 °C for different times from 3 to 60 min, followed by water quenching. This IA temperature corresponds to the maximum austenite fraction determined (by X-ray diffraction) in a previous work for the same steel [15] (note that the cold rolling procedure is different here). The different annealing time selected here is to produce different levels of grain sizes (from submicron level to above 1 µm) and austenite mechanical stability, without any substantial changes of the other phase parameters (e.g. fraction, composition, morphology and the degree of recrystallization).

2.2. Tensile testing and in situ correlative DIC and magnetic induction experiments

Room temperature uniaxial tensile tests were conducted for the intercritically annealed samples at a constant crosshead speed corresponding to an initial strain rate of $\sim 8 \times 10^{-4} \text{ s}^{-1}$. The ASTM E-8 subsize standard sample (25 mm gage length) was used, and three tensile specimens were tested for each annealing condition. The strain value was recorded using an extensometer. The yield point elongation was acquired from the engineering stress-strain curve, by subtracting the strain at upper yield point from the strain point of discontinuous yielding to uniform strain hardening transition. In order to investigate the Lüders band properties and its interaction with deformation-induced martensite transformation, we designed a novel *in situ* correlative DIC and magnetic induction experiment. This enables an integrated analysis of local strain and local martensite formation in the same sample during tensile testing. The experimental setup is shown in Fig. 1 (a). A G-504 Manta digital camera (AI-lid Vision Technologies GmbH, Stadtroda, Germany) with a telecentric lens was placed on one side of the tensile specimen. The field of view covers the whole gage section and the numerical spatial resolution is around $7 \mu\text{m}/\text{pixel}$. Images were acquired at a rate of 4 frames per second. The local strain fields were then computed using the in-house OpenDIC software [26] and post-processed with the image analysis program Fiji [27]. The magnetic induction experiment implemented by a Feritscope (Fischer, FMP 30) was used to measure the local austenite change due to α' -martensite formation during tensile testing. The Feritscope probe was placed on the other side of the tensile sample and tightly attached to the center (Fig. 1 (a)), and the

value was recorded every 2.5 s. The austenite fraction measured by the Feritscope was calibrated in advance using the synchrotron X-ray diffraction results (will be described in Section 2.3).

2.3. In situ synchrotron high-energy X-ray diffraction measurement and data analysis

The *in situ* synchrotron high-energy X-ray diffraction (HE-XRD) experiments during tensile deformation were conducted on the beamline P02.1 of PETRA III at Deutsches Elektronen-Synchrotron Center (DESY) in Hamburg, Germany. The experimental setup is described in Fig. 1 (b). The beamline was operated at a fixed energy of $\sim 60 \text{ keV}$, which corresponds to a monochromatic X-ray with a wavelength of $\sim 0.20738 \text{ \AA}$. The beam size is $0.5 \times 0.5 \text{ mm}^2$. The attached quasi-static tensile testing was carried out on a Kammrath & Weiss stress rig with a constant crosshead speed of 0.72 mm/min . A dog-bone shape tensile specimen with a gage length of 12 mm and width of 2 mm was used [28]. Note that the extensometer was not used here, and only the applied tensile load and crosshead displacement were recorded. Two-dimensional diffraction patterns were collected by a PerkinElmer fast area detector every 1 s during tensile testing. The detector distance and instrument broadening were calibrated by a standard CeO_2 sample. The Debye-Scherrer diffraction rings were then analyzed and three types of information were obtained:

- Phase identification and volume fraction. The diffraction intensity was integrated over the whole azimuth range ($0^\circ \sim 360^\circ$) using the Fit2D software [29]. Five crystallographic reflections of FCC ($\{111\}$, $\{200\}$, $\{220\}$, $\{311\}$, $\{222\}$) and four

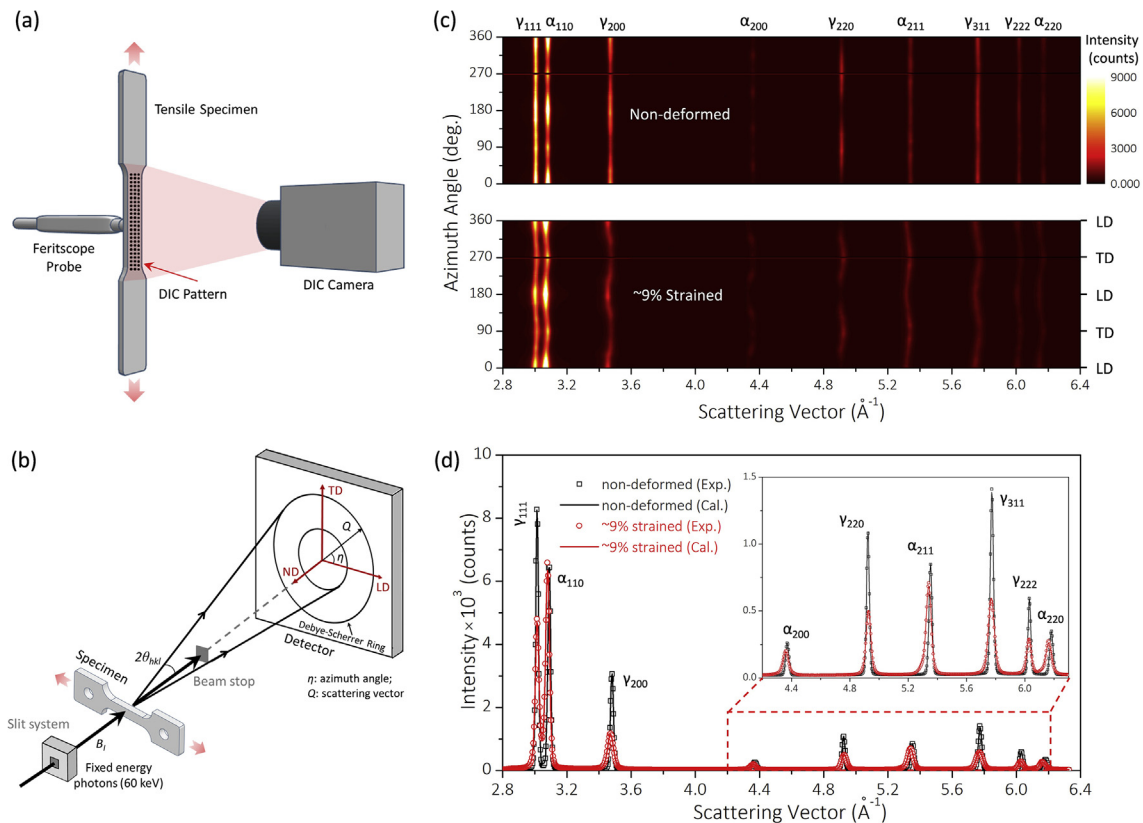


Fig. 1. Schematic sketch showing (a) the experimental setup of the *in situ* correlative DIC and magnetic induction measurement and (b) the setup of the *in situ* synchrotron high-energy X-ray diffraction [28]; (c) Diffraction intensity plotted as a function of Azimuth angle and scattering vector, for the 5 min annealed sample with non-deformed condition and deformed condition at the applied strain of $\sim 9\%$ (corresponding to the completion of Lüders band propagation); (d) Integrated intensity as a function of scattering vector for the samples in (c) (both experimental data (Exp.) and calculated results (Cal.) using the Rietveld refinement method are shown).

reflections of BCC ($\{110\}$, $\{200\}$, $\{211\}$, $\{220\}$) were identified. The volume fraction of austenite was analyzed using the Rietveld refinement method with the aid of the MAUD software [30]. Fig. 1 (c) and (d) demonstrate two typical diffraction intensity maps plotted as a function of Azimuth angle and scattering vector and the corresponding integral one-dimensional diffraction patterns, respectively. The blank regions around the azimuth angle of 270° in Fig. 1 (c) are due to the nontransparent holder of beam stop. Both experimental diffraction patterns and the calculated results by the Rietveld refinement are presented in Fig. 1 (d).

- (b) Lattice strain along the loading direction (LD). The *in situ* diffraction rings were first azimuthally integrated into 36 sectors (10° per sector). The sector along LD (centered at the azimuth angle of 0°) was taken to analyze the lattice strain. Each integral diffraction peak was fitted by a Gaussian function in order to determine the interplanar spacing (d) and lattice parameter (a) [10]. Both the lattice strain for each diffraction plane (ϵ_{hkl}) and the weighted average lattice strain for each phase ($\bar{\epsilon}_p$) were calculated, using the following equations [8,10]:

$$\epsilon_{hkl} = (d_{hkl}^\sigma - d_{hkl}^0) / d_{hkl}^0 \quad (1)$$

$$\bar{\epsilon}_p = (\bar{a}_p^\sigma - \bar{a}_p^0) / \bar{a}_p^0 \quad (2)$$

where d_{hkl}^σ and d_{hkl}^0 are the interplanar spacing of the sample under loading and prior to loading, respectively; \bar{a}_p^σ and \bar{a}_p^0 are the weighted average lattice parameter [10] of each phase for the loaded and unloaded sample, respectively.

- (c) Peak width. Relative changes of the diffraction peak width (i.e. peak broadening) are normally attributed to the inhomogeneous microstrain induced by dislocation-like defects

and/or the shrinkage of the coherent scattering volume [25,31,32]. Both factors indicate subgrain-scaled activities caused by plastic deformation [31]. The full width at half maximum (FWHM) was determined here by single peak fitting to characterize the peak width for each reflection.

2.4. Microstructural characterization

The microstructure was characterized using electron backscatter diffraction (EBSD) and electron channeling contrast imaging (ECCI) [33] (a JEOL JSM-6500F SEM for EBSD and a Zeiss-Merlin SEM for ECCI). The acquired EBSD data (phase, orientation, fraction, grain size and the degree of recrystallization) was analyzed using the TSL OIM software package. The fraction of recrystallized grains was determined based on the analysis of grain orientation spread (GOS), under the criterion that recrystallized grains have a GOS value less than 2° [34]. The average austenite composition (Mn, Al and Si) was quantified by Energy-Dispersive X-Ray Spectroscopy (EDX) point analysis, performed in a JEOL JSM-6500F SEM. The analysis was performed on larger austenite crystal clusters (above $\sim 2 \mu\text{m}$) containing several austenite grains, in order to minimize the effect of the surrounding ferrite phase. The micro/nano-scaled microstructural evolution under deformation was investigated using *in situ* three-point bending testing combined with ECCI and EBSD, placing particular emphasis on the early plastic deformation regime. The sample used for the bending tests was a rectangular sheet with a dimension of $7 \text{ mm} \times 4 \text{ mm} \times 1.4 \text{ mm}$.

3. Results

3.1. Microstructure

The microstructure of the intercritically annealed samples is shown in Fig. 2, with more detailed phase information (fraction,

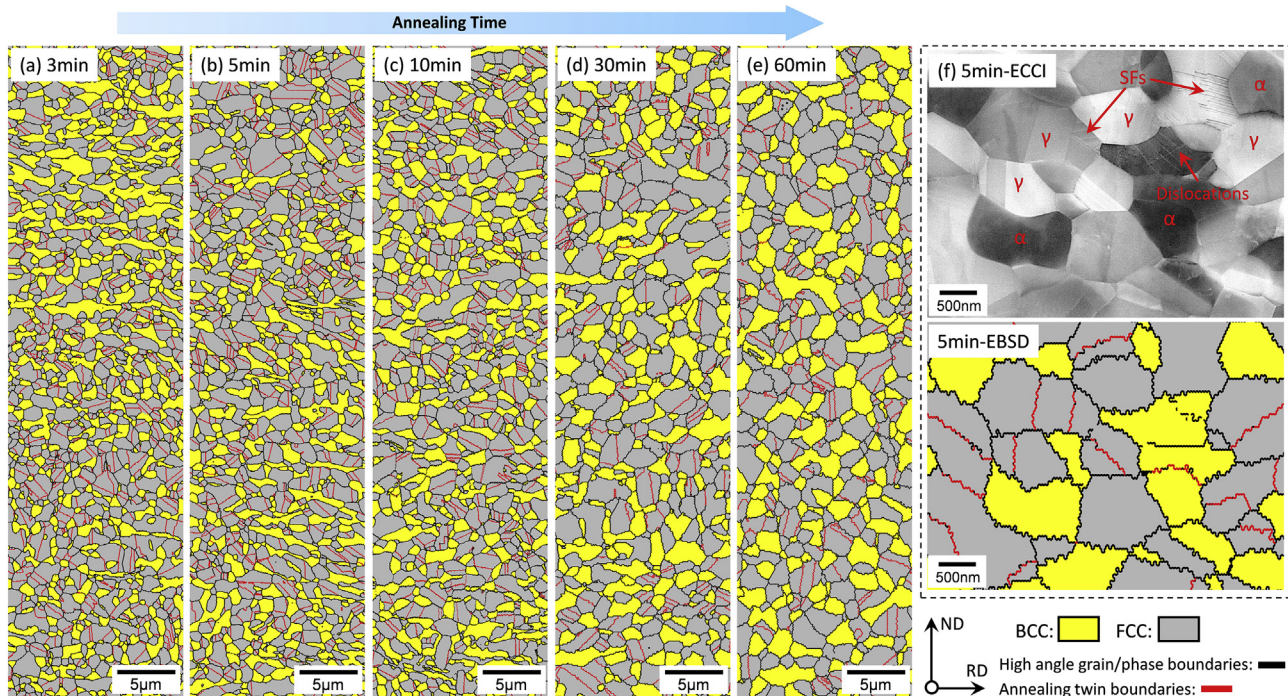


Fig. 2. EBSD phase mapping of the steel samples intercritically annealed at 800°C for (a) 3 min, (b) 5 min, (c) 10 min, (d) 30 min and (e) 60 min; (f) Correlative ECCI and EBSD results for the 5 min annealed sample, showing a fully recrystallized microstructure with a few stacking faults (SFs) inside austenite and dislocations in ferrite.

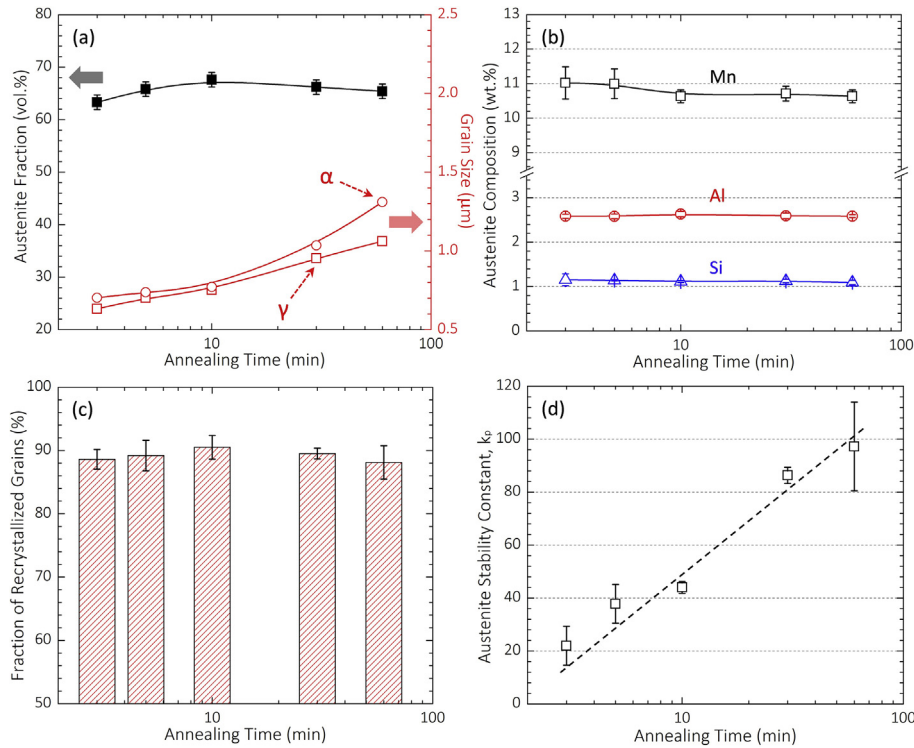


Fig. 3. (a) Austenite fraction and sample grain size (generated from EBSD results), (b) austenite Mn, Al and Si contents and (c) the fraction of recrystallized grains (determined by EBSD) of the intercritically annealed samples (annealing temperature 800 °C), as a function of annealing time; (d) Austenite stability constant (k_p) of the intercritically annealed samples at different annealing times, determined based on *in situ* magnetic induction measurement and the Ludwigson-Berger analysis [38].

size, austenite composition and the fraction of recrystallized grains) presented in Fig. 3 (a)–(c). An austenite plus ferrite duplex microstructure with globular grains is formed after intercritical annealing (Fig. 2 (a)–(e)). The microstructure is almost fully recrystallized with only a few stacking faults (SFs) and dislocations, as revealed by ECCI (Fig. 2 (f)). The average density of dislocations was estimated to be around 5.7×10^{12} and $5.9 \times 10^{12} \text{ m}^{-2}$ for the samples annealed for 3 and 60 min, respectively, based on ECCI observations of more than 50 individual grains for each sample. Details of the dislocation density measurement by ECCI can be found elsewhere [35]. All the intercritically annealed samples have an austenitic matrix, with its fraction of around 65 vol%. The annealing time does not substantially influence the austenite fraction (Fig. 3 (a)), the Mn, Al and Si contents of austenite (Fig. 3 (b)) and the degree of recrystallization (Fig. 3 (c)). The similar phase fraction among different samples also indicates a similar austenite C content, suggested by the lever rule, given the very limited C solubility in ferrite [36,37]. The grain size of both austenite and ferrite increases with annealing time, from $\sim 650 \text{ nm}$ after 3 min annealing to slightly above $1 \mu\text{m}$ after 60 min annealing. The increase of the austenite grain size results in a reduction of austenite mechanical stability. This is supported by the change of the austenite stability constant (k_p), which was determined based on the Ludwigson-Berger analysis [7,38]: $1/V_\gamma - 1/V_{\gamma 0} = (k_p/p)\epsilon^p$, where ϵ is macroscopic true strain, V_γ and $V_{\gamma 0}$ are austenite fraction at ϵ strain and 0 strain, respectively, p is the strain exponent (taken as 1 [7]). The change of the austenite fraction as a function of strain was measured by the *in situ* magnetic induction method. The determined k_p value of the intercritically annealed samples is shown in Fig. 3 (d). It increases with higher annealing times (larger grain sizes), confirming a continuously decreased austenite mechanical stability.

3.2. Tensile and Lüders banding behavior

The engineering stress-strain curve and the behavior of the deformation-induced martensite formation are shown in Fig. 4 (a)–(c). The changes of strain hardening, tensile strength and ductility with annealing time are associated with the different degrees of the TRIP effect controlled by the austenite mechanical stability. This has been well documented in the literature [6,39] for similar steels and is not the main focus here. All the investigated samples show a distinct discontinuous yielding behavior, accompanying the appearance of Lüders bands. The propagation of the Lüders bands through the Feritscope analyzed area results in a strain-induced martensite burst at small macroscopic strain levels (below 5%, as shown in Fig. 4 (b) and (c)). Fig. 4 (c) shows that with increasing annealing time, the YPE value decreases while the martensite formation during yielding (i.e. the average value of the first martensite plateau) increases. Such interaction is plotted more clearly in Fig. 4 (d). For the samples with lower austenite stability (i.e. samples annealed for 30 and 60 min), the martensite fraction starts to increase immediately after load is applied. This means that the initial portion of the martensite in these samples is stress-induced. However, these samples still show discontinuous yielding. This differs from some previous literature [3,8] which reported a continuous yielding behavior for medium Mn steels undergoing stress-induced martensite transformation.

The details of the Lüders banding mapped by DIC for the samples annealed for 5, 30 and 60 min are shown in Fig. 5–7. Some band properties are listed in Table 1. For the 5 min annealed sample (Fig. 5), a Lüders band nucleates approximately at the center of the specimen with a local strain of $\sim 5\%$ (Fig. 5 (c)) and local strain rate of $\sim 1.4 \times 10^{-2} \text{ s}^{-1}$ (Fig. 5 (a) and Table 1). It comprises two band fronts and propagates towards both sides along the tensile axis. The

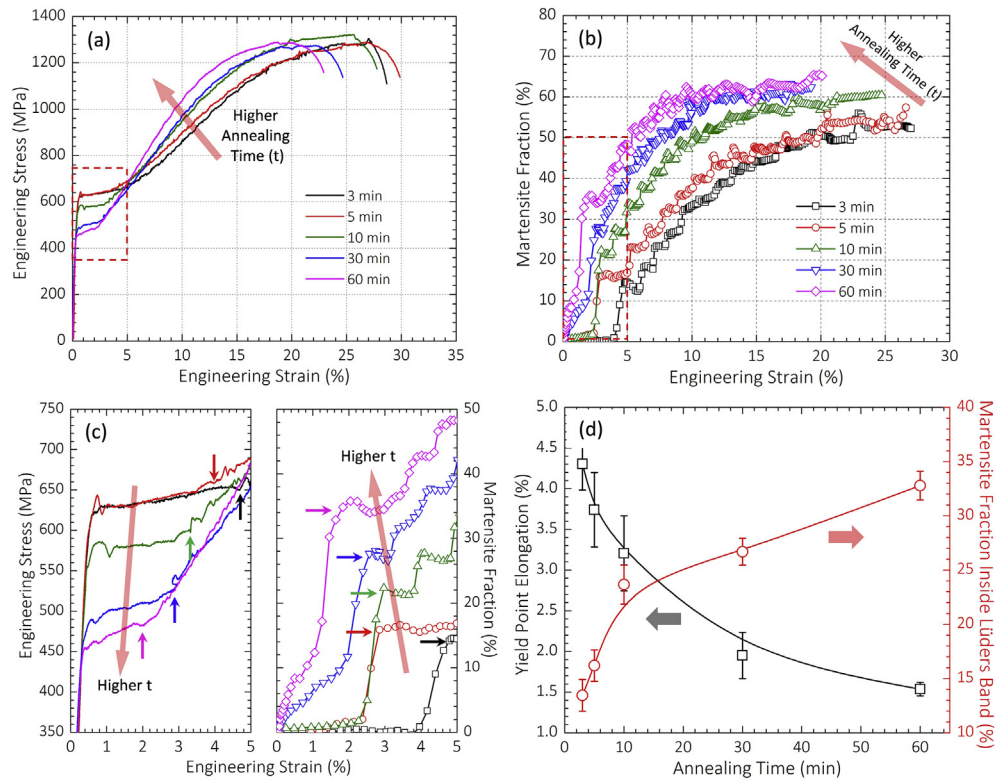


Fig. 4. (a) Engineering stress-strain curve and (b) deformation-induced martensite formation of the samples intercritically annealed at 800 °C for different annealing times from 3 to 60 min; (c) Magnified curves taken from the rectangular frames in (a) and (b), showing the detailed behavior of the yielding stage (both the end of the discontinuous yielding stage and the first martensite plateau are marked by solid arrows with different colors); (d) Change of yield point elongation and the deformation-induced martensite fraction formed during yielding as a function of annealing time. (For interpretation of the references to color in this figure legend, the reader is referred to the Web version of this article.)

Table 1

Some properties of the Lüders bands mapped by DIC for the samples annealed for 5, 30 and 60 min (the grain size and austenite stability constant are also listed).

Annealing time (min)	Grain size (μm)		Austenite stability constant (k_p)	Lüders strain (%)	Lüders strain rate ($\times 10^{-2} \text{ s}^{-1}$)	Number of band fronts	Band propagation velocity (mm/s)	Angle between Lüders band and tensile axis (deg.)
	γ	α						
5	0.70	0.74	37.8	4.9	1.4	2	0.30–0.61	59.5
30	0.95	1.03	86.3	3.4	0.9	4	0.32–0.56	68.8
60	1.06	1.31	97.2	2.6	0.6	>4	0.58	78.2

propagation velocity of the upper band front (0.42–0.61 mm/s) is higher than that of the lower one (0.3–0.45 mm/s). The propagation of each band front does not always show a continuous pattern due to their mutual competition. For example, the lower band front stops propagating at about 21s starting from nucleation, at which the upper band front propagates faster (0.61 mm/s). It then continues to spread at about 27s when the propagation of the upper band front is almost complete (Fig. 5 (a)–(c)). This derives from the difference of the local stress required to move each band front. Regarding the deformation-induced martensite formation, Fig. 5 (d) demonstrates a simultaneous and sudden increase of local strain and local martensite fraction inside the area probed by the Feritscope. This observation provides a direct evidence that martensite forms inside the Lüders band and its formation is induced by the high local strain.

For the longer time (30 and 60 min) annealed specimens with larger grain size and lower austenite mechanical stability, the local strain and strain rate inside the Lüders bands drop (Table 1), translating to a lower YPE value (Fig. 4 (d)). In addition, a higher number of nucleation sites for Lüders bands is observed, as shown

in Fig. 6–7. This is especially notable for the 60 min annealed specimen (Fig. 7), where the band front at the lower part of the gage section cannot even be identified. The banding behavior at this location is dominated by continuous band nucleation and mutual merging, i.e. approaching a uniform/continuous yielding behavior. With respect to the band propagation behavior, the average velocity does not change much with higher annealing times (0.3–0.61, 0.32–0.56 and 0.58 mm/s for the 5 min, 30 min and 60 min annealed sample, respectively). The band fronts seem to become more diffuse for the longer annealed samples, as suggested by the increasing angle between the Lüders band and tensile axis (Fig. 5–7 and Table 1). The interaction between microstructure and the Lüders banding behavior will be discussed in Section 4.2.

3.3. Micromechanical behavior tracked by in situ synchrotron HE-XRD

In order to reveal the underlying mechanisms of discontinuous yielding in the investigated steels, the initiation of the plastic deformation in each phase needs to be understood. The 5 min

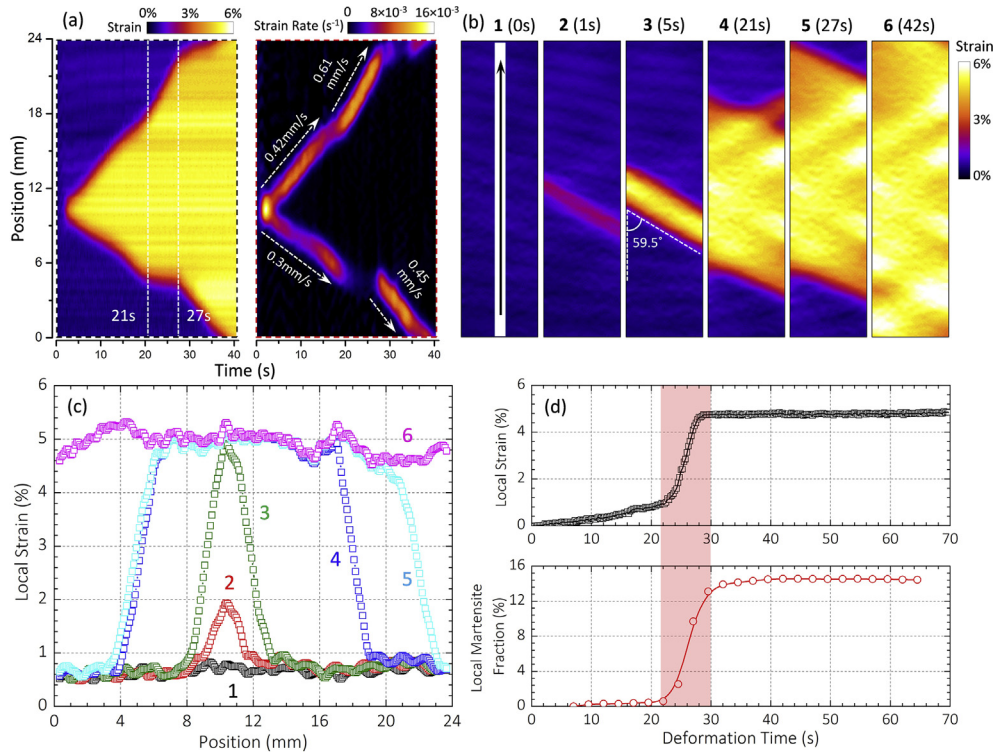


Fig. 5. Lüders banding behavior for the sample annealed at 800 °C for 5 min: (a) Time evolution of the local strain and strain rate along the tensile axis (only the yielding stage is shown; the time point just before Lüders band nucleation is set as 0 s; the velocity of each band front at different propagation stages is added); (b) Selected local strain maps covering the whole gage section, showing the formation and propagation of Lüders bands; (c) Corresponding one-dimensional local strain profiles along the tensile axis (the area where the strain profiles were taken is marked in (b)); (d) Time evolution of the local strain and local martensite fraction inside the Feritscope analyzed area (the x-axis here is the real deformation time).

annealed sample was selected for this purpose. We start the analysis from the *in situ* HE-XRD experiment, which probes the microscopic deformation behavior of each phase with high grain statistics. The engineering stress-strain curve acquired from the HE-XRD tensile stage is shown in Fig. 8 (a) and (b). Note that since extensometer was not used here, the strain was determined from the crosshead displacement. The deformation can be divided into three stages before the completion of Lüders band propagation (at ~9% strain):

Stage I (elastic stage, 0–3.8% strain): the stress increases linearly with applied engineering strain. The material deforms elastically within this stage.

Stage II (elastic-plastic transition, 3.8–4.6% strain): this regime starts from the time when the curve deviates from linearity (at ~3.8% strain), which can be identified by the drop of the slope (Fig. 8 (b)). In this stage, microyielding occurs suggesting that some of the grains are plastically deformed.

Stage III (Lüders band nucleation and propagation, 4.6–9% strain): the start of this stage is the time when the upper yield stress is achieved (at ~4.6% strain), which is considered roughly to be the nucleation stress for the Lüders bands [40–42].

The change of austenite fraction, lattice strain and peak width of austenite and ferrite in the three deformation stages are presented in Fig. 8 (c), Fig. 9 (a)–(b) and Fig. 9 (c), respectively. Due to the high angular resolution of synchrotron HE-XRD, overlapping diffraction peaks of ferrite and strain-induced tetragonal α' -martensite can in principle be separated [10,25,43]. For the investigated steel, the asymmetry of the BCC diffraction peaks due to such a peak overlapping effect can indeed in some cases be observed, provided that the volume fraction of α' -martensite is above a certain value (~1.2 vol% for {200} planes and ~8.2 vol% for {211} planes,

corresponding to the applied strain of ~7.1 and ~7.4%, respectively). However, here we study only the initiation regime of plastic deformation in the two phases, which occurs within the elastic-plastic transition stage (Stage II). The amount of α' -martensite formed in this deformation regime is very small (below 0.3 vol%, Fig. 8 (c)), which renders peak separation and analysis of asymmetry features in HE-XRD diffraction peaks error-prone. Therefore, for the results presented in Fig. 9, peak separation was not performed and the lattice strain and peak width of ferrite were determined by single peak fitting ignoring the slight peak asymmetry at relatively high strain levels (above ~7%) [10].

At Stage I, the sample is deformed elastically, hence the lattice strain increases linearly with applied strain and the peak width maintains constant (Fig. 9 (a)–(c)). The austenite fraction also does not change in this regime, which supports the results shown in Fig. 4 (c) that no stress-induced martensite is formed in the sample annealed for 5 min.

Within the elastic-plastic transition (i.e. microyielding) stage (Stage II), the austenite lattice strain for all planes deviates from linear behavior at certain points and shows a decreasing slope with applied strain (Fig. 9 (a)). This is also evident for the average lattice strain of austenite shown in Fig. 9 (b). For a better assessment of the slope change, the 1st derivative of the average phase lattice strain versus applied macroscopic strain was plotted and placed as an inset in Fig. 9 (b). It is found that the slope change for austenite occurs at ~3.8% strain, which is the same as the strain value for the onset of deformation Stage II. The peak width of austenite for all the lattice planes shows an increasing trend in this deformation regime (Fig. 9 (c)). All of these findings suggest that austenite starts to be plastically deformed immediately at the start point of the macroscopic elastic-plastic transition stage. The total austenite fraction in

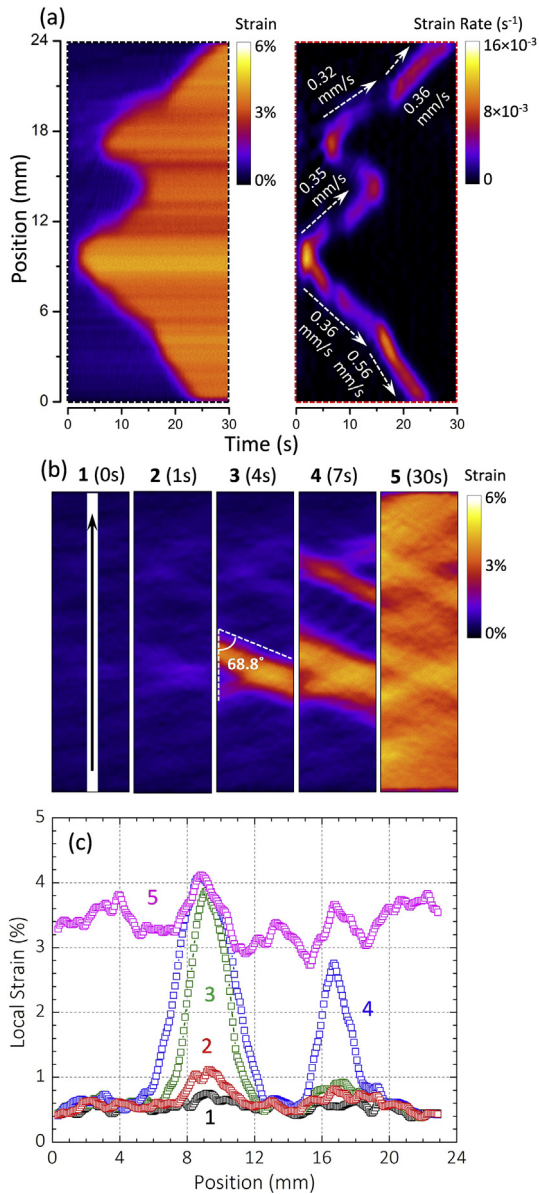


Fig. 6. Lüders banding behavior for the sample annealed at 800°C for 30 min: (a) Time evolution of the local strain and strain rate along the tensile axis (the velocity of each band front at different propagation stages is added); (b) Selected local strain maps covering the whole gage section, showing the formation and propagation of Lüders bands; (c) Corresponding one-dimensional local strain profiles along the tensile axis (the area where the strain profiles were taken is marked in (b)).

Fig. 8 (c) also shows a very slight decrease (below $\sim 0.3 \text{ vol}\%$) at this deformation stage, implying that martensite is formed by the plastic deformation inside some austenite grains. With respect to ferrite, both the lattice strain for $\{110\}$, $\{211\}$ and $\{220\}$ planes (Fig. 9 (a)) and the average lattice strain (Fig. 9 (b)) exhibit a much later slope decrease (at the applied strain of $\sim 4.3\%$, Fig. 9 (b)) compared with austenite. This indicates that ferrite in the current alloy is harder than austenite, thus the onset of plastic deformation of ferrite occurs later. The results agree well with some of the literature [36] for similar alloys where a higher hardness value was reported in the ferrite phase. It is noted that the α_{200} plane shows a slope increase at around 4% strain (Fig. 9 (a)), which can thus be explained by the load partitioning from the plastically softer austenite to the harder ferrite [44]. The peak widths for the α_{110} , α_{211} and α_{220} lattice planes do not show much change at this

deformation stage, indicating that the plastic deformation in ferrite is small or only confined in a few ferrite grains. This observation also implies that the ferrite-martensite peak overlap is subtle for these three ferrite lattice planes. However, the peak overlap seems affecting the α_{200} planes whose peak width is observed to be increased from the beginning of deformation Stage II (Fig. 9 (c)).

In Stage III, the nucleated Lüders bands start to propagate along the gage length. The austenite fraction shown in Fig. 8 (c) exhibits a sudden decrease at the applied strain between $\sim 6.8\%$ and $\sim 7.8\%$, whereas no obvious change can be observed at other strain levels in this deformation regime. Since strain-induced α' -martensite forms locally inside Lüders bands (Fig. 5 (d)), this observation suggests that the bands only propagate through the HE-XRD detected area from 6.8 to 7.8% strain. Within this macroscopic strain range, the lattice strains and peak widths for both austenite and ferrite also change substantially (Fig. 9 (a) and (c)). The lattice strains for certain austenite planes ($\{111\}$, $\{220\}$, $\{311\}$ and $\{222\}$) show a decreasing trend at the applied strain levels from 6.8 to 7.8% (Fig. 9 (a)). This could be due to the internal compressive stress resulting from the martensite transformation and the resulting volume expansion (about 3–4% for Fe–C steels at room temperature [45]). This point has been validated numerically by Gibbs et al. [8] assuming that the transformation follows the Bain lattice correspondence.

3.4. Deformation micromechanisms revealed by *in situ* three-point bending test

In order to further investigate the deformation micromechanisms of each phase and their interactions, an *in situ* three-point bending test combined with EBSD and ECCL with nano-scaled resolution was performed on the same sample (5 min annealed specimen). The macroscopic images at different deformation states (undeformed (D0) as well as deformation regimes 1 (D1), 2 (D2), 3 (D3) and 4 (D4)) are shown in Fig. 10 (a). We focus on the region with the highest tensile stress (the intersection between the center of the loading point and the upper surface, as shown in Fig. 10 (a)) in order to correlate with the results from HE-XRD. The tensile strain of this region corresponding to the D3 state is below 1%, much lower than the Lüders strain of this sample (4.9%, Table 1). Comparison of the EBSD results in this region between the D0 state and D3 state shows that the overall fraction of deformation-induced martensite formed in this stage is almost negligible. This observation supports the assumption that the tensile deformation imposed by the current bending test before the D3 state is within the elastic stage or the elastic-plastic transition stage. The tensile strain corresponding to the D4 state is about 1.7%.

We selected three microscopic areas to track the microstructural evolution: Area 1 mainly focuses on austenite (Fig. 10 (b)); Area 2 mainly focuses on ferrite (Fig. 10 (c)); Area 3 is a larger area revealing both austenite and ferrite deformation (Fig. 11). The plastic deformation of austenite is observed in the D1 state (Fig. 10 (b) and 11, marked by arrows). Both, gliding of initial partial dislocations causing stacking faults extension (γ_3 in Fig. 10 (b) and γ_1 and γ_4 in Fig. 11) and new stacking faults formation (γ_1 in Fig. 10 (b) and γ_2 in Fig. 11) are observed. EBSD plane trace analysis shows that all the partial dislocations glide along $\{111\}$ planes. On the other hand, no plastic flow in ferrite has been observed at this deformation state, neither in the three areas presented nor in any other observed regions containing in total more than 20 ferrite grains. This finding matches the *in situ* HE-XRD results, namely, austenite plastically deforms before the ferrite phase in the microplastic regime. Upon further deformation, more stacking faults are formed either from the original slip systems or newly activated systems (D2 state in Fig. 10 (b) and 11 (c)). α' -martensite tends to nucleate at

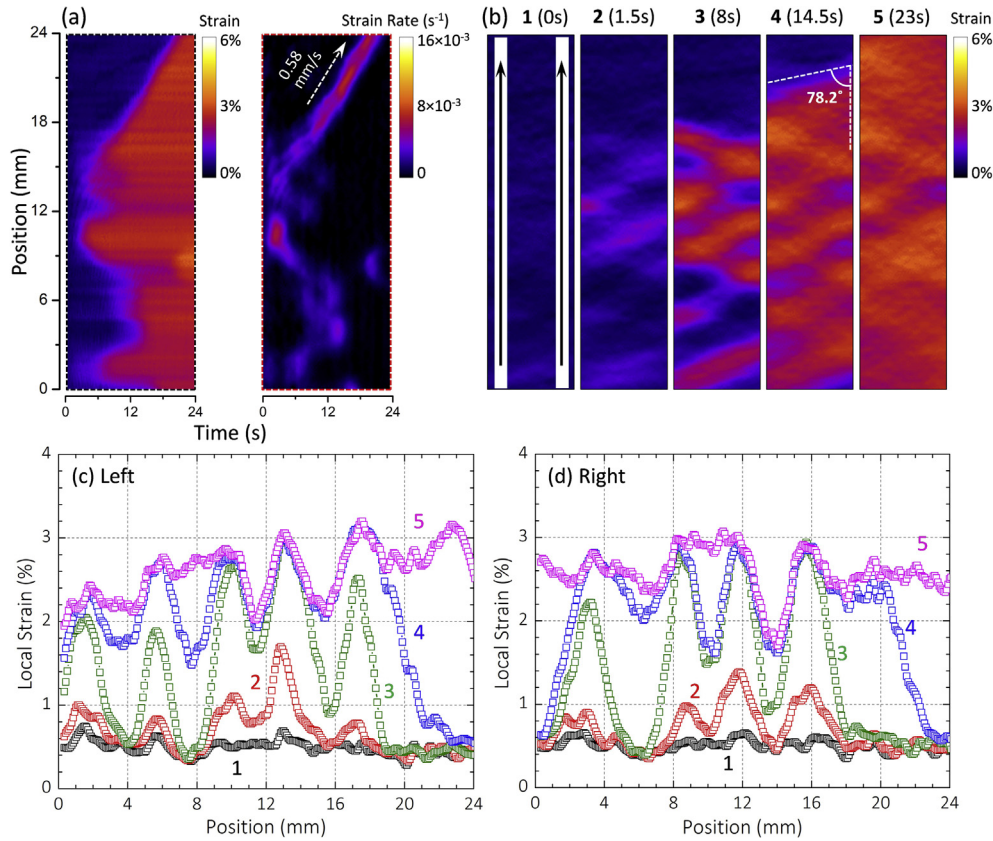


Fig. 7. Lüders banding behavior for the sample annealed at 800°C for 60 min: (a) Time evolution of the local strain and strain rate along the tensile axis (the velocity of each band front at different propagation stages is added); (b) Selected local strain maps covering the whole gage section, showing the formation and propagation of Lüders bands; (c) and (d) are the corresponding one-dimensional local strain profiles taken from the left and right rectangular area in (b), respectively.

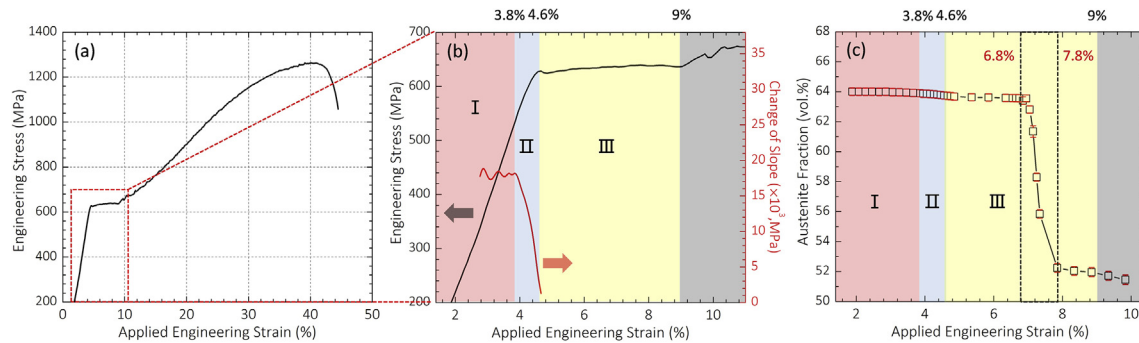


Fig. 8. (a) Engineering stress as a function of applied engineering strain for the 5 min annealed sample (acquired from the synchrotron HE-XRD tensile stage; note that the extensometer was not used here, as such the strain was determined from the crosshead displacement); (b) Magnified curve taken from the rectangular frame in (a), plotted with the change of the slope up to the upper yield point (1st derivative of the engineering stress versus engineering strain); (c) Change of the retained austenite fraction with tensile straining for the same sample, determined by the synchrotron HE-XRD and the Rietveld refinement method.

various interacting shearing systems (D3 state in Fig. 10 (b) and 11 (d)), e.g. stacking faults intersections or stacking faults-annealing twin intersections. The so formed martensite follows a Kurdjumov-Sachs (K–S) or Nishiyama-Wassermann (N–W) orientation relationships (OR) with the parent austenite (analyzed using EBSD data, Fig. 11 (d)).

The deformation of ferrite only occurs after the deformation state of D2 (Fig. 10 (c)). It is found that a large number of full dislocations are generated at some α - γ interfaces and glide into ferrite grains (D2–D4 in Figs. 10 (c) and Fig. 11 (d)). Sometimes partial

dislocations are simultaneously emitted at the same interfaces and glide into the austenite side (D2–D3 in Fig. 10 (c)). This suggests that α - γ interfaces serve as preferable dislocation nucleation sites for both ferrite and austenite. In other circumstances, stacking faults form first crossing the whole austenite grains. Then dislocations are emitted into ferrite from the intersections between these stacking faults and interfaces (Fig. 11 (d)), in order to relieve the accumulated stresses due to dislocation pileups [46]. Dislocation nucleation from the interface areas and the resulting rapid increase in the mobile dislocation density are believed to be the major reason for

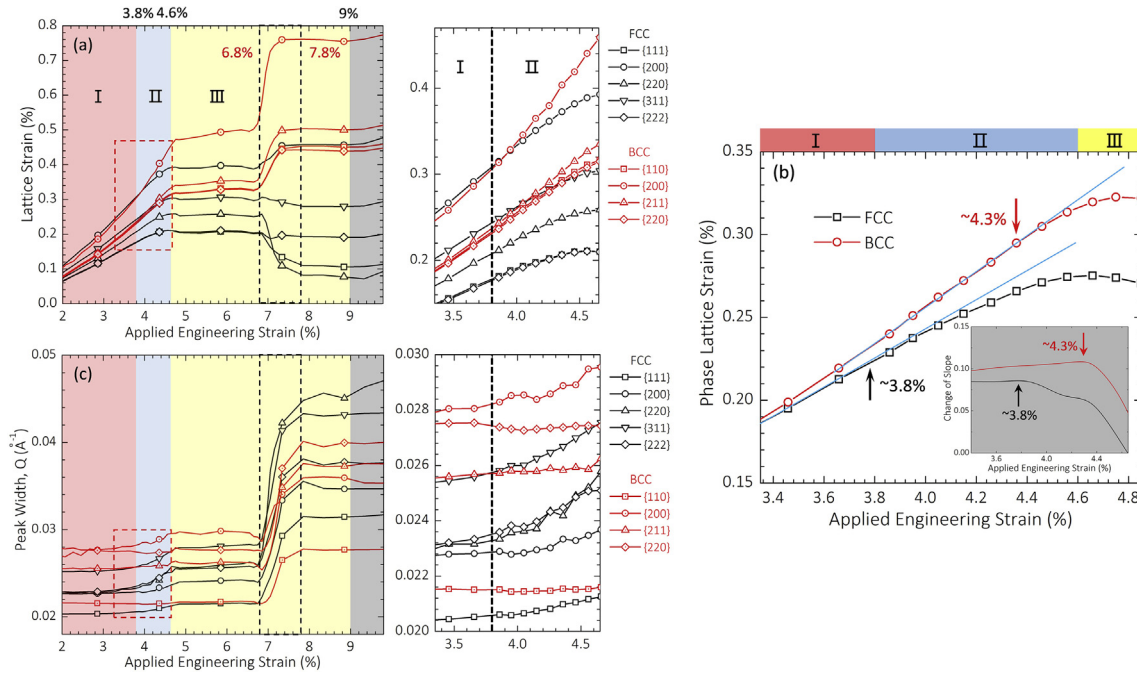


Fig. 9. (a) Change of the lattice strain and (c) peak width for each crystallographic reflection as a function of applied engineering strain (for each figure, the curve in deformation Stage II is magnified and shown on the right side); (b) Change of the weighted average lattice strain for both FCC and BCC as a function of applied engineering strain (the 1st derivative of the phase lattice strain versus applied strain, i.e. the change of slope, is also inset in this figure).

the discontinuous yielding in medium Mn steels. This point will be further discussed in Section 4.1.

4. Discussion

In this section, we first discuss the dislocation-based origin of discontinuous yielding in medium Mn steels. The discussion in this part relies on the information of the plastic deformation initiation of the two phases within the microyielding or elastic-plastic transition stage, which has been probed by the *in situ* synchrotron HE-XRD and three-point bending experiments. In the second part of the discussion, we relate the proposed micromechanism to some macroscopic parameters of the Lüders bands and discuss the influence of the deformation-induced martensite formation on the banding behavior.

4.1. Origin of discontinuous yielding in medium Mn steels

Regardless of the different dislocation mechanisms for discontinuous yielding (e.g. locking-unlocking [16,18] or dislocation multiplication mechanisms [19,22]), two essential conditions are required: (a) an initially low density of mobile dislocations and (b) a rapid dislocation multiplication (or an avalanching-driven increase in the number of mobile dislocations). The Cottrell-Bilby mechanism is generally proposed for single phase ferritic steels where the binding energy between interstitials and dislocations is high [16,18]. However, here we show that medium Mn steels with an austenite matrix (~65 vol%) can exhibit pronounced discontinuous yielding (Section 3.2), which leads to the question whether the Cottrell-Bilby mechanism (especially the dislocation unlocking process) is indeed dominant here. Both *in situ* synchrotron HE-XRD and three-point bending tests shown in Sections 3.3–3.4 provide an unambiguous evidence that austenite is the phase that is plastically deformed first (in the microyielding stage). Then before dislocation unlocking from the hypothetical Cottrell atmospheres in ferrite, the

plastic deformation of austenite would already provide certain amounts of fresh mobile dislocations. This is unfavorable for the occurrence of discontinuous yielding in the bulk medium Mn steels if such phenomenon is driven by the Cottrell mechanism. Further, the Cottrell mechanism also fails to explain the absence of discontinuous yielding in austenite-ferrite medium Mn steels with a large fraction (~50%) of δ -ferrite [15,37] or with a laminated microstructure morphology [2,5]. In the latter case, a higher dislocation density is always found in lamellar ferrite due to inactive recrystallization [2]. However, based on the calculation from Cottrell and Bilby [16], a C level as low as 10^{-4} wt% would be able to lock all the dislocations in ferrite with a dislocation density as high as that in tempered martensite (the order of 10^{14} m^{-2} [47]).

From a theoretical perspective, it has been accepted for many metals that the dislocation velocity (v) increases monotonously with the applied stress (σ), following [19,23]:

$$v = (\sigma/\sigma_0)^n \quad (3)$$

Where σ_0 is a reference stress and n is a constant. For a constant applied strain rate ($\dot{\epsilon}$), the following relation will be expected:

$$\dot{\epsilon}_U = \rho_m^U b v_U = \dot{\epsilon}_L = \rho_m^L b v_L \quad (4)$$

where ρ_m and b are the density and Burgers vector of mobile dislocations, respectively, and the super/sub-script U and L indicate the value at the upper and lower yield point, respectively. Based on Eqs. (3) and (4), the difference between the upper and lower yield stress (i.e. the yield drop) will depend on the increase of mobile dislocations between upper and lower yield points (i.e. $\sigma_U/\sigma_L = (\rho_m^L/\rho_m^U)^{1/n}$). This suggests that if the Cottrell mechanism is dominant, a more pronounced yield drop should be expected with increasing ferrite fraction due to more unlocking dislocations. However, this trend has not been observed when here we study two other cold rolled medium Mn steels with compositions of

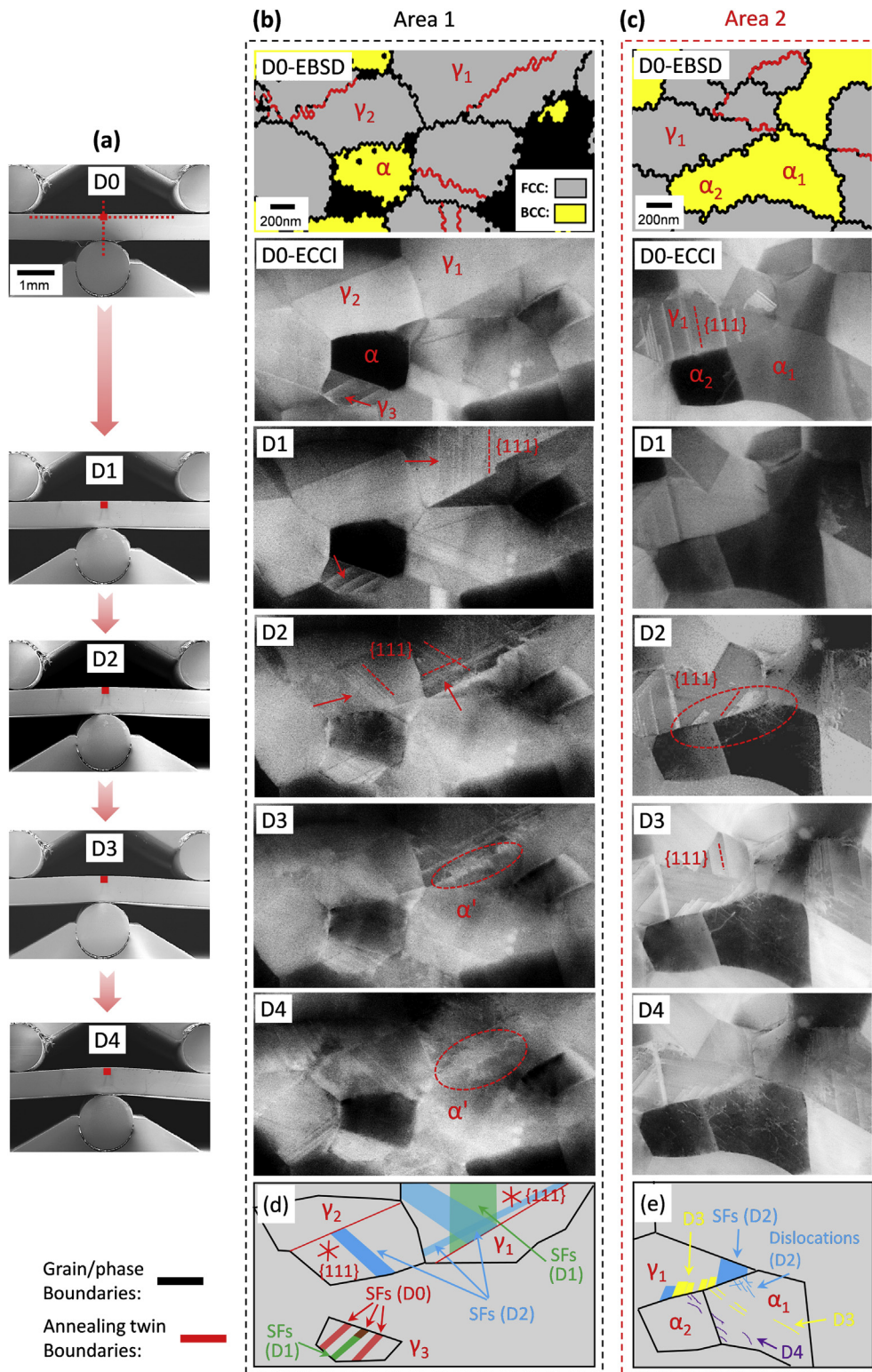


Fig. 10. (a) Macroscopic secondary electron (SE) images for the 5 min annealed specimen under *in situ* three-point bending tests (different deformation states are marked by D0, D1, D2, D3 and D4, which donates undeformed condition as well as deformation regimes 1, 2, 3, 4, respectively); Microstructural evolution of the same sample upon bending deformation: (b) selected Area 1 and (c) selected Area 2 (the two areas were taken from the region marked by a solid rectangle in (a), where the maximum tensile stress is concentrated); (d) and (e) Schematic diagram showing the evolution of planar defects (stacking faults or dislocations) ((d) was drawn based on (b, D0–D3) and (e) was drawn based on (c, D0–D4)).

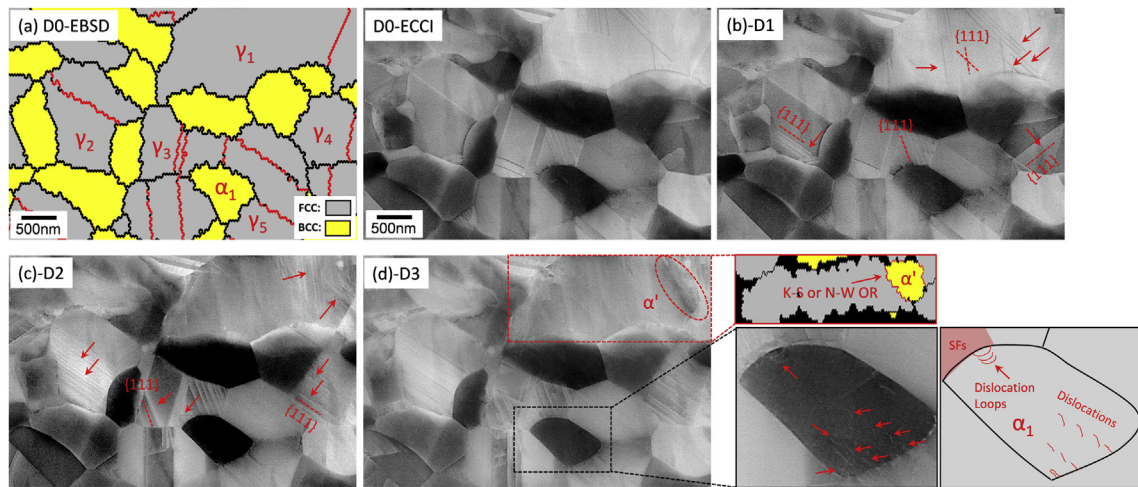


Fig. 11. Microstructural evolution in selected Area 3 taken from the same specimen and same region in Fig. 10: (a) undeformed state, (b) deformation state 1, (c) deformation state 2 and (d) deformation state 3 with a corresponding EBSD phase map showing the α' -martensite formation and a magnified ECC image for a ferrite grain. (The formation of stacking faults and dislocations is marked by arrows; In (d), the phase boundary owning a K–S or N–W orientation relationship (OR) is marked by red lines in the EBSD map.). (For interpretation of the references to color in this figure legend, the reader is referred to the Web version of this article.)

0.2C–7Mn–3Al and 0.2C–10Mn–3Al (in wt.%). More specific, we heat treated these two steels at a same intercritical annealing condition (750 °C for 5 min). The different Mn contents result in different ferrite volume fractions (~20% higher in the steel containing 7 wt% Mn), and the same annealing condition ensures a similar grain size and recrystallization extent. The same tensile setup was used for identical machine stiffness. More than 10 tensile specimens were repeated for each steel, in order to minimize the effect of any possible misalignment. The determined yield drop (i.e. σ_U / σ_L) is around 1.02 for both steels, which is obviously not sensitive to phase fractions.

The insensitivity of the yield drop to phase fractions also supports the idea that the possible Suzuki mechanism in austenite should not be the dominant factor for discontinuous yielding either. In fact, the absence of discontinuous yielding in well annealed high-Mn austenitic steels [48] with a similar austenitic deformation behavior as the current study already suggests the Suzuki locking is not active. On the other hand, it has been shown in Section 3.4 that new stacking faults from various slip systems form in austenite at the start of its plastic deformation. This means that the unlocking of the initial partial dislocations from the hypothetical Suzuki atmospheres and their further gliding are not necessarily required for the deformation of austenite.

The above discussion exhibits the limits of the locking-unlocking mechanisms for explaining discontinuous yielding in medium Mn steels. In Figs. 10 and 11, we show that the α - γ interfaces act as preferable nucleation sites for new partial dislocations in austenite and for full dislocations in ferrite, which can be attributed to two factors. Firstly, the difference in elastic and plastic properties between the two phases enhances the stress concentration at the interface region. Secondly, in ultrafine grained materials, dislocation generation from Frank-Read sources is difficult due to the reduced dislocation segment length and the strong influence of dislocation back stresses. In this case, the interface boundary ledges can be more favorable to nucleate dislocations [49–51]. However, such nucleation process still needs to overcome an energy barrier [49], which makes the nucleation stress higher than the stress needed for dislocation gliding. This stress difference would contribute to the occurrence of discontinuous yielding. Further, given the ultrafine grain scale in the investigated steels, the total α - γ interface area is very large. For example, EBSD analysis of

the 5 min annealed sample shows that the length of the interface is 5.6 mm (for a measurement area of $2.6 \times 10^{-3} \text{ mm}^2$), much larger than the total length of all other types of boundaries (3.4 mm, including grain and twin boundaries). This effect provides a high density of dislocation sources, which can result in a very rapid increase in density of freshly formed mobile dislocations. Based on the model proposed by Johnston and Gilman [19,22,23], the rapid dislocation multiplication would favor discontinuous yielding.

The other requirement for discontinuous yielding, i.e. initially low mobile dislocation density, can also be fulfilled due to the ultrafine grain size. Some papers suggested that high angle boundaries can act as sinks for dislocations via atomic shuffling and free volume reorganization inside boundaries [52,53]. The initially formed mobile dislocations can thus be trapped by the high number of interface boundaries. Although this dislocation absorption process has been mostly discussed for nanocrystalline materials with grain sizes below 100 nm [53], it might occur and influence the macroscopic mechanical properties also of materials with slightly larger grain sizes. One hint for this effect is that a significant decrease of work hardening has been observed when the grain size is reduced down to ~1 μm for both austenitic [54] and ferritic steels [55,56], which can be a direct consequence of dislocation absorption at boundaries [56,57]. Here we observe in Fig. 10 (c) (γ_1 in D0 and D1 state) that some initial stacking faults have disappeared at the very beginning of austenite deformation. This might be considered as a support for the dislocation absorption process at the interface (if dislocations have not glided towards the sample surface and disappeared there). It can also be argued that various locking atmospheres (e.g. Cottrell and Suzuki) do exist and all the initial dislocations are permanently locked by them. However, we believe that this is not the case here at least for the austenite because gliding of initial partial dislocations does occur (Fig. 10 (b) and 11).

The discussion thus suggests that one dominant factor governing discontinuous yielding in austenite–ferrite duplex medium Mn steels is the grain size, which needs to be small enough to provide a large interface area, thus providing a high density of dislocation sources. This can well explain the aforementioned insensitivity of the occurrence of discontinuous yielding and the yield drop on phase fractions. It also elucidates the absence of discontinuous yielding in medium Mn steels containing coarse δ -ferrite with a

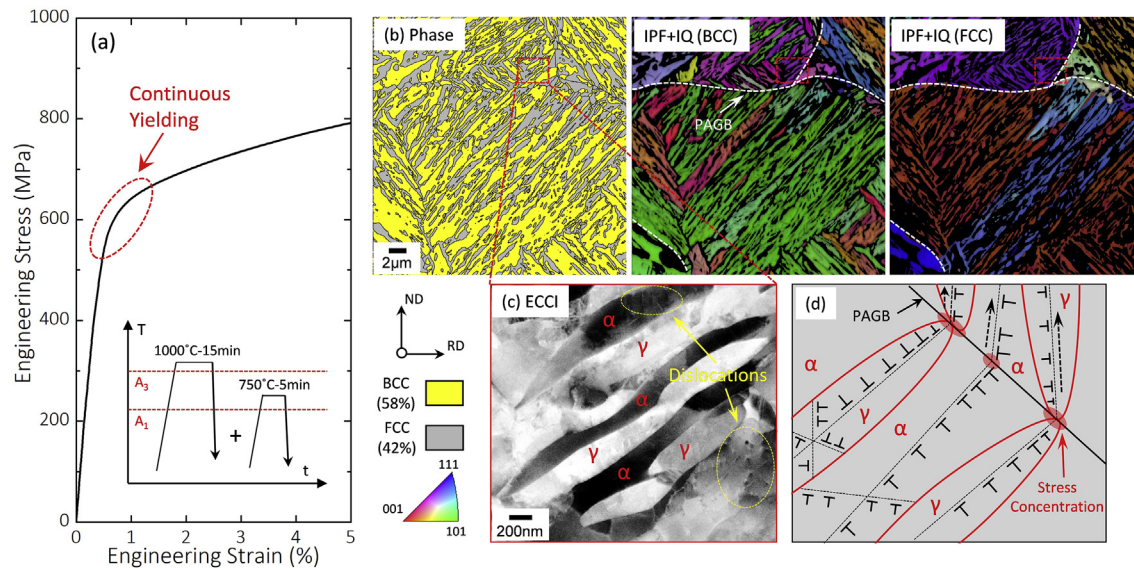


Fig. 12. (a) Engineering stress-strain curve showing the continuous yielding of the same medium Mn steel processed to have a laminated microstructure morphology (only the strain up to 5% is shown, and the heat treatment schedule is also inset); (b) EBSD phase, image quality (IQ) and inverse pole figure (IPF) mapping of the same sample in (a), showing the laminated austenite plus ferrite microstructure; (c) Magnified ECCI taken from the rectangular frame in (b), showing the grown-in dislocations; (d) Schematic sketch illustrating the dislocation behavior during the yielding stage, which is proposed to account for the continuous yielding (PAGB represents prior austenite grain boundary).

grain size normally above 10 μm [37]. We can also apply the current findings to explain the yielding behavior of steels with a laminated microstructure morphology. One typical example of this type of microstructure showing continuous yielding is demonstrated in Fig. 12. The same steel was subjected to a first annealing treatment at the austenization temperature (1000 $^{\circ}\text{C}$ for 15 min) followed by water quenching, to form a fully martensitic structure. A second intercritical annealing was then conducted at 750 $^{\circ}\text{C}$ to produce a laminated austenite and ferrite structure (Fig. 12 (b) and (c)), with a typical lamellar width below 500 nm. The lamellar length is above 10 μm , which is controlled by the prior austenite grain boundary (PAGB) and by the block size of the fresh martensite formed after the first annealing. The dislocation density is higher in this type of structure (Fig. 12 (c)) compared with the globular structure which is normally fully recrystallized (Figs. 2 (f) and Fig. 3 (c)). This is one factor reducing the tendency of discontinuous yielding if the dislocations are initially mobile and their number is high enough to exceed the absorbing capacity of the interface boundaries [19,22]. Here we propose another view in addition to this point, based on the reduced density of dislocation sources (schematically shown in Fig. 12 (d)). It is expected that the number of pileup dislocations will be higher on the slip plane nearly parallel to the lamellar direction than on the perpendicular ones. The difference can be quite enormous given the high aspect ratio of the lamellae. This will produce a much higher stress concentration at the lamella tips, and dislocations nucleate preferably at these regions. Therefore, the effective number of dislocation sources and the rate of dislocation density increase can be remarkably reduced, compared to steels with globular microstructures. This is another important factor contributing to continuous yielding in laminated medium Mn steels.

Current experimental results and discussion show that dislocation nucleation from the α - γ interfaces and the resulting rapid increase in the number of mobile dislocations can be utilized as a central reason accounting for discontinuous yielding in medium Mn steels. It is important to mention that here we mainly argue about the occurrence of dislocation unlocking and its role on discontinuous yielding. Although the dislocation locking process by the Cottrell atmosphere (if existed) is in the current case not

necessary for discontinuous yielding, it would essentially provide one additional mechanism for immobilizing grown-in dislocations in ferrite, thus providing more favorable conditions for discontinuous yielding. This indicates that there might still be some effects of interstitial atoms (here C) on the yielding behavior in such steels. More importantly in the current case, C segregating at the phase boundaries might have some influence on dislocation nucleation [17,58,59]. Such segregation has been observed in our previous study for a 0.2C–10Mn–3Al–3Si steel [37]. Takaki et al. [58] proposed that segregated C atoms might stabilize the dislocation source at interface boundaries, based on an overview of the Hall-Petch coefficients in ferritic steels with different C levels and heat treatment conditions. The atomic mechanism could be that C atoms increase the difficulty of atomic reordering inside interfaces which is necessary for dislocation emission [60]. Russell et al. [61] also calculated the binding energy of a C atom in a grain boundary based on an Eshelby-type analysis and found it to be about equal to the binding energy between C and dislocations. These findings suggest that C segregation might enhance the stress difference between dislocation nucleation and its further gliding, thus promoting the appearance of discontinuous yielding. This point needs further investigations though.

4.2. Influence of deformation-induced martensite on the yielding behavior

It has been shown in Section 3.2 that the Lüders strain exhibits a monotonous decrease with larger grain size and decreased mechanical stability of austenite. Such effect of grain size has also been documented in many single phase materials [62,63]. The underlying micromechanism was proposed as that the deformation at the Lüders band front is easier to spread grain by grain with a larger size due to the higher amounts of pileup dislocations and the associated stress concentrations (i.e. the Hall-Petch relation). Based on the discussion in Section 4.1, a more straightforward explanation can be established in the current steels. A larger grain size will result in a lower dislocation multiplication rate (due to a smaller interface area), thus a lower dislocation density inside Lüders bands which contributes to a lower Lüders strain.

Here we mainly discuss the influence of deformation-induced martensite formation controlled by the austenite mechanical stability on the observed Lüders banding behavior. The respective effects of strain- and stress-induced martensite are separated here. Strain-induced martensite forms inside Lüders bands. This occurs in all the investigated samples and the amount increases with lower austenite stability (i.e. higher annealing times, Fig. 4 (c)). The transformation relies on the local strain increase (i.e. formation of various interacting shearing systems in austenite, Figs. 10 and 11). Therefore, strain-induced martensite should not have a critical role on Lüders band nucleation, but rather affect the band propagation due to the increase of local work hardening rate. The relationship between Lüders strain ϵ_L , band propagation velocity v_L , and number of Lüders fronts n can be expressed by the following equation [64]:

$$\epsilon_L = s/nv_L \quad (5)$$

Where s is the crosshead speed (here 1.5 mm/min). The equation shows that for the same material with a fixed value of Lüders strain, the increase of Lüders band fronts will result in a reduction of band velocity. However, here we found that the band propagation velocity maintains similar with annealing time (Table 1), despite the increasing number of band fronts. This strongly suggests that for the longer time annealed sample, a higher local work hardening rate must be obtained to sustain the band velocity. This increased work hardening is provided by the higher amounts of strain-induced martensite forming inside the Lüders bands.

On the other hand, stress-induced martensite formation only occurs for samples with a very low austenite stability (i.e. 30 and 60 min annealed samples). It happens immediately starting with the onset of tensile loading (Fig. 4 (c)), well before the microplastic deformation of any of the phases. The transformation would provide fresh mobile dislocations and promote plastic flow, which will then affect the nucleation of Lüders bands. Here we show that with higher amounts of stress-induced martensite, the number of potential nucleation sites for Lüders bands increases (Figs. 6 and 7). Due to the presence of stress concentrations and local differences in austenite stability [65], stress-induced martensite might not form uniformly throughout the tensile specimen. Therefore, the multiple Lüders band nucleation sites can be explained by the preferable plastic deformation at the locations where stress-induced martensite transformation occurs. It can then be expected, if austenite stability becomes even lower and stress-induced martensite forms throughout the whole specimen, that plastic deformation would become more uniform, thus achieving continuous yielding. This is validated in Fig. 13, in which the sample is annealed for a longer time (2 h at 800 °C) to further decrease the austenite mechanical stability. The finding suggests that a critical value of stress-induced martensite should be achieved to fully eliminate discontinuous yielding.

It should be noted that the respective influence of deformation-induced martensite and grain size on the yielding behavior cannot be further separated, because larger grain size normally results in lower austenite stability which has been demonstrated in the present study and in other reports [66,67]. Nevertheless, we can conclude here that both factors should have a critical influence due to their crucial roles on the formation of mobile dislocations and/or for local work hardening rate.

5. Conclusions

The present study investigated the yielding mechanisms in ultrafine austenite-ferrite duplex medium Mn steels, based on various *in situ* microstructural characterization techniques from macroscopic down to nanoscopic scale. The main conclusions are as

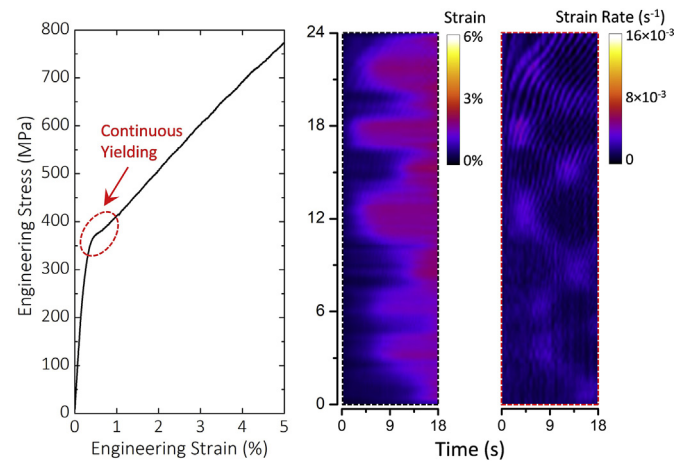


Fig. 13. Engineering stress-strain curve and the corresponding time evolution of the local strain and strain rate along the tensile axis, for the same medium Mn steel annealed at 800 °C for 2 h to produce a lower austenite stability and a higher amount of stress-induced martensite. The sample exhibits a near continuous yielding behavior, with plastic deformation initiating more uniformly throughout the specimen.

follows:

- (1) We demonstrated that medium Mn steels with an austenite matrix (65 vol%) can show a distinct discontinuous yielding phenomenon. *In situ* synchrotron-based HE-XRD experiments revealed that both austenite and ferrite were plastically deformed before the macroscopic upper yield point (referred to as microyielding). The microplastic deformation started in austenite before ferrite yielded, which was also validated by *in situ* three-point bending experiments in concert with ECCI and EBSD. The deformation micro-mechanism of austenite at the beginning of plastic flow consisted of the gliding of grown-in partial dislocations along {111} planes causing stacking faults extension and fresh formation of stacking faults. The austenite-ferrite interfaces acted as preferable nucleation sites for new partial dislocations in austenite and for full dislocations in ferrite. The large total interface area, due to the ultrafine grain size, could provide a high density of dislocation sources and result in a rapid increase of mobile dislocations, which was believed to be the major reason accounting for the occurrence of discontinuous yielding. This finding also provided a more robust explanation for several other yielding phenomena in duplex medium Mn steels as compared with the traditional locking-unlocking mechanisms (e.g. Cottrell-Bilby and Suzuki theories). These include the relative insensitivity of the yield drop on phase fractions, as well as the absence of discontinuous yielding in medium Mn steels with coarse δ -ferrite or a laminated microstructure morphology.
- (2) Yield point elongation and the Lüders strain decreased with higher annealing times which produced a larger grain size and thus a lower mechanical stability of austenite. Other phase characteristics (fraction, composition, morphology and dislocation density) remained almost intact with selected different annealing conditions. A novel *in situ* correlative DIC and magnetic induction experiment was designed and utilized to probe the Lüders banding behavior and the local deformation-induced martensite formation inside Lüders bands. Multiple band fronts were observed in the investigated samples. Their number increased with longer annealing times, whereas their average propagation velocity remained similar. These observations were

interpreted by the critical influence of the grain size and the amount of stress-/strain-induced martensite on mobile dislocation generations and/or local work hardening rate.

Acknowledgements

Part of this work is supported by the Deutsche Forschungsgemeinschaft (DFG) within the Collaborative Research Center (SFB) 761 “Steel-ab initio”, which is gratefully acknowledged. The authors gratefully acknowledge the synchrotron X-ray diffraction experiment (Proposal No.: I-20170777) support at beamline P02.1 of PETRA III at DESY, a member of the Helmholtz Association (HGF). The authors also acknowledge Prof. S. Yue from McGill University and Dr. F. Fazeli and Dr. C. Scott from CanmetMATERIALS, Canada, for providing the materials. R.S. Varanasi gratefully acknowledges IMPRS SurMat for the financial support. B. Sun gratefully acknowledges the research fellowship provided by the Alexander von Humboldt Foundation.

References

- [1] S. Lee, B.C. De Cooman, Annealing temperature dependence of the tensile behavior of 10 pct Mn multi-phase TWIP-TRIP steel, *Metall. Mater. Trans. A* 45 (2014) 6039–6052.
- [2] J. Han, S.J. Lee, J.G. Jung, Y.K. Lee, The effects of the initial martensite microstructure on the microstructure and tensile properties of intercritically annealed Fe-9Mn-0.05 C steel, *Acta Mater.* 78 (2014) 369–377.
- [3] B.C. De Cooman, P. Gibbs, S. Lee, D.K. Matlock, Transmission electron microscopy analysis of yielding in ultrafine-grained medium Mn transformation-induced plasticity steel, *Metall. Mater. Trans. A* 44 (2013) 2563–2572.
- [4] H. Luo, H. Dong, M. Huang, Effect of intercritical annealing on the Lüders strains of medium Mn transformation-induced plasticity steels, *Mater. Des.* 83 (2015) 42–48.
- [5] J. Han, S.H. Kang, S.J. Lee, Y.K. Lee, Fabrication of bimodal-grained Al-free medium Mn steel by double intercritical annealing and its tensile properties, *J. Alloy. Comp.* 681 (2016) 580–588.
- [6] B. Sun, F. Fazeli, C. Scott, B. Guo, C. Aranas, X. Chu, M. Jahazi, S. Yue, Microstructural characteristics and tensile behavior of medium manganese steels with different manganese additions, *Mater. Sci. Eng., A* 729 (2018) 496–507.
- [7] K. Steineder, D. Krizan, R. Schneider, C. Beal, C. Sommitsch, On the microstructural characteristics influencing the yielding behavior of ultra-fine grained medium-Mn steels, *Acta Mater.* 139 (2017) 39–50.
- [8] P.J. Gibbs, B. De Cooman, D.W. Brown, B. Clausen, J.G. Schroth, M.J. Merwin, D.K. Matlock, Strain partitioning in ultra-fine grained medium-manganese transformation induced plasticity steel, *Mater. Sci. Eng., A* 609 (2014) 323–333.
- [9] X. Wang, B. He, C. Liu, C. Jiang, M. Huang, Extraordinary Lüders-strain-rate in medium Mn steels, *Materialia* 6 (2019) 100288.
- [10] K. Yan, K.D. Liss, I.B. Timokhina, E.V. Pereloma, In situ synchrotron X-ray diffraction studies of the effect of microstructure on tensile behavior and retained austenite stability of thermo-mechanically processed transformation induced plasticity steel, *Mater. Sci. Eng., A* 662 (2016) 185–197.
- [11] J. Kadkhodapour, S. Schmauder, D. Raabe, S. Ziaei-Rad, U. Weber, M. Calcagnotto, Experimental and numerical study on geometrically necessary dislocations and non-homogeneous mechanical properties of the ferrite phase in dual phase steels, *Acta Mater.* 59 (2011) 4387–4394.
- [12] J.Y. Choi, J. Lee, K. Lee, J.Y. Koh, J.H. Cho, H.N. Han, K.T. Park, Effects of the strain rate on the tensile properties of a TRIP-aided duplex stainless steel, *Mater. Sci. Eng., A* 666 (2016) 280–287.
- [13] M. Zhang, R. Li, J. Ding, H. Chen, J.S. Park, J. Almer, Y.-D. Wang, In situ high-energy X-ray diffraction mapping of Lüders band propagation in medium-Mn transformation-induced plasticity steels, *Materials Research Letters* 6 (2018) 662–667.
- [14] B. He, Z. Liang, M. Huang, Nanoindentation investigation on the initiation of yield point phenomenon in a medium Mn steel, *Scr. Mater.* 150 (2018) 134–138.
- [15] B. Sun, F. Fazeli, C. Scott, N. Brodusch, R. Gauvin, S. Yue, The influence of silicon additions on the deformation behavior of austenite-ferrite duplex medium manganese steels, *Acta Mater.* 148 (2018) 249–262.
- [16] A.H. Cottrell, B. Bilby, Dislocation theory of yielding and strain ageing of iron, *Proc. Phys. Soc. Sect. A* 62 (1949) 49–62.
- [17] D. Wilson, Grain-size dependence of discontinuous yielding in strain-aged steels, *Acta Metall.* 16 (1968) 743–753.
- [18] H. Suzuki, Chemical interaction of solute atoms with dislocations, science reports of the research institutes, tohoku university, Ser. A, Physics, chemistry and metallurgy 4 (1952) 455–463.
- [19] G.T. Hahn, A model for yielding with special reference to the yield-point phenomena of iron and related bcc metals, *Acta Metall.* 10 (1962) 727–738.
- [20] J. Wilde, A. Cerezo, G. Smith, Three-dimensional atomic-scale mapping of a Cottrell atmosphere around a dislocation in iron, *Scr. Mater.* 43 (2000) 39–48.
- [21] M. Herbig, D. Raabe, Y. Li, P. Choi, S. Zaefferer, S. Goto, Atomic-scale quantification of grain boundary segregation in nanocrystalline material, *Phys. Rev. Lett.* 112 (2014) 126103.
- [22] W.G. Johnston, Yield points and delay times in single crystals, *J. Appl. Phys.* 33 (1962) 2716–2730.
- [23] W.G. Johnston, J.J. Gilman, Dislocation velocities, dislocation densities, and plastic flow in lithium fluoride crystals, *J. Appl. Phys.* 30 (1959) 129–144.
- [24] X. Wang, L. Wang, M. Huang, Kinematic and thermal characteristics of Lüders and Portevin-Le Châtelier bands in a medium Mn transformation-induced plasticity steel, *Acta Mater.* 124 (2017) 17–29.
- [25] M. Zhang, L. Li, J. Ding, Q. Wu, Y.D. Wang, J. Almer, F. Guo, Y. Ren, Temperature-dependent micromechanical behavior of medium-Mn transformation-induced-plasticity steel studied by in situ synchrotron X-ray diffraction, *Acta Mater.* 141 (2017) 294–303.
- [26] N. Vanderesse, M. Lagacé, F. Bridier, P. Bocher, An open source software for the measurement of deformation fields by means of digital image correlation, *Microsc. Microanal.* 19 (2013) 820–821.
- [27] J. Schindelin, I. Arganda-Carreras, E. Frise, V. Kaynig, M. Longair, T. Pietzsch, S. Preibisch, C. Rueden, S. Saalfeld, B. Schmid, Fiji: an open-source platform for biological-image analysis, *Nat. Methods* 9 (2012) 676–682.
- [28] Y. Ma, W. Song, W. Bleck, Investigation of the microstructure evolution in a Fe-17Mn-1.5 Al-0.3 C steel via in situ synchrotron X-ray diffraction during a tensile test, *Materials* 10 (2017) 1129.
- [29] A. Hammersley, FIT2D: a multi-purpose data reduction, analysis and visualization program, *J. Appl. Crystallogr.* 49 (2016) 646–652.
- [30] L. Lutterotti, S. Matthies, H. Wenk, MAUD: a friendly java program for material analysis using diffraction, *CPD Newsletter IUCr* 21 (1999) 14–15.
- [31] X. Zhang, M. Li, J.S. Park, P. Kenesei, J. Almer, C. Xu, J.F. Stubbins, In situ high-energy X-ray diffraction study of tensile deformation of neutron-irradiated polycrystalline Fe-9% Cr alloy, *Acta Mater.* 126 (2017) 67–76.
- [32] L. Wang, M. Li, J. Almer, Investigation of deformation and microstructural evolution in Grade 91 ferritic-martensitic steel by in situ high-energy X-rays, *Acta Mater.* 62 (2014) 239–249.
- [33] I. Gutierrez-Urrutia, S. Zaefferer, D. Raabe, Coupling of electron channeling with EBSD: toward the quantitative characterization of deformation structures in the SEM, *JOM* 65 (2013) 1229–1236.
- [34] D. Field, L. Bradford, M. Nowell, T. Lillo, The role of annealing twins during recrystallization of Cu, *Acta Mater.* 55 (2007) 4233–4241.
- [35] E. Breitbarth, S. Zaefferer, F. Archie, M. Besel, D. Raabe, G. Requena, Evolution of dislocation patterns inside the plastic zone introduced by fatigue in an aged aluminium alloy AA2024-T3, *Mater. Sci. Eng., A* 718 (2018) 345–349.
- [36] S. Lee, S. Shin, M. Kwon, K. Lee, B.C. De Cooman, Tensile properties of medium Mn steel with a bimodal UFG α - γ and coarse δ -ferrite microstructure, *Metall. Mater. Trans. A* 48 (2017) 1678–1700.
- [37] B. Sun, D. Palanisamy, D. Ponge, B. Gault, F. Fazeli, C. Scott, S. Yue, D. Raabe, Revealing fracture mechanisms of medium manganese steels with and without delta-ferrite, *Acta Mater.* 164 (2019) 683–696.
- [38] D. Ludwigson, J.A. Berger, Plastic behaviour of metastable austenitic stainless steels, *J. Iron Steel Inst* 207 (1969) 63–69.
- [39] Q. Han, Y. Zhang, L. Wang, Effect of annealing time on microstructural evolution and deformation characteristics in 10Mn1.5Al TRIP steel, *Metall. Mater. Trans. A* 46 (2015) 1917–1926.
- [40] J.C. Suits, B. Chalmers, Plastic microstrain in silicon-iron, *Acta Metall.* 9 (1961) 854–860.
- [41] S. Nagarajan, R. N. V. B. Advanced imaging for early prediction and characterization of zone of Lüders band nucleation associated with pre-yield microstrain, *Mater. Sci. Eng., A* 561 (2013) 203–211.
- [42] D.W. Moon, T. Vreeland Jr., The initiation of yielding in silicon-iron, *Acta Metall.* 17 (1969) 989–996.
- [43] N. Jia, Z. Cong, X. Sun, S. Cheng, Z. Nie, Y. Ren, P. Liaw, Y. Wang, An in situ high-energy X-ray diffraction study of micromechanical behavior of multiple phases in advanced high-strength steels, *Acta Mater.* 57 (2009) 3965–3977.
- [44] O. Muránsky, P. Sittner, J. Zrník, E. Oliver, In situ neutron diffraction investigation of the collaborative deformation–transformation mechanism in TRIP-assisted steels at room and elevated temperatures, *Acta Mater.* 56 (2008) 3367–3379.
- [45] J. Moyer, G. Ansell, The volume expansion accompanying the martensite transformation in iron-carbon alloys, *Metall. Trans. A* 6 (1975) 1785.
- [46] T. Lee, I. Robertson, H. Birnbaum, TEM in situ deformation study of the interaction of lattice dislocations with grain boundaries in metals, *Philos. Mag.* A 62 (1990) 131–153.
- [47] S. Takebayashi, T. Kunieda, N. Yoshinaga, K. Ushioda, S. Ogata, Comparison of the dislocation density in martensitic steels evaluated by some X-ray diffraction methods, *ISIJ Int.* 50 (2010) 875–882.
- [48] D.T. Pierce, J.A. Jiménez, J. Bentley, D. Raabe, J.E. Wittig, The influence of stacking fault energy on the microstructural and strain-hardening evolution of Fe-Mn-Al-Si steels during tensile deformation, *Acta Mater.* 100 (2015) 178–190.
- [49] L. Capolungo, D. Spearot, M. Cherkaoui, D. McDowell, J. Qu, K. Jacob, Dislocation nucleation from bicrystal interfaces and grain boundary ledges: relationship to nanocrystalline deformation, *J. Mech. Phys. Solids* 55 (2007) 2300–2327.
- [50] L. Murr, Dislocation ledge sources: dispelling the myth of Frank-Read source

- importance, *Metall. Mater. Trans. A* 47 (2016) 5811–5826.
- [51] J. Li, Y. Chou, The role of dislocations in the flow stress grain size relationships, *Metall. Mater. Trans. B* 1 (1970) 1145.
 - [52] A. Hasnaoui, P.M. Derlet, H. Van Swygenhoven, Interaction between dislocations and grain boundaries under an indenter—a molecular dynamics simulation, *Acta Mater.* 52 (2004) 2251–2258.
 - [53] M.A. Meyers, A. Mishra, D.J. Benson, Mechanical properties of nanocrystalline materials, *Prog. Mater. Sci.* 51 (2006) 427–556.
 - [54] F. Yan, G. Liu, N. Tao, K. Lu, Strength and ductility of 316L austenitic stainless steel strengthened by nano-scale twin bundles, *Acta Mater.* 60 (2012) 1059–1071.
 - [55] N. Tsuji, N. Kamikawa, R. Ueji, N. Takata, H. Koyama, D. Terada, Managing both strength and ductility in ultrafine grained steels, *ISIJ Int.* 48 (2008) 1114–1121.
 - [56] K.T. Park, D.H. Shin, Microstructural interpretation of negligible strain-hardening behavior of submicrometer-grained low-carbon steel during tensile deformation, *Metall. Mater. Trans. A* 33 (2002) 705–707.
 - [57] O. Bouaziz, Y. Estrin, Y. Brechet, J. Embury, Critical grain size for dislocation storage and consequences for strain hardening of nanocrystalline materials, *Scr. Mater.* 63 (2010) 477–479.
 - [58] S. Takaki, D. Akama, N. Nakada, T. Tsuchiyama, Effect of grain boundary segregation of interstitial elements on Hall–Petch coefficient in steels, *Mater. Trans.* 55 (2014) 28–34.
 - [59] J.-H. Kang, S. Duan, S.J. Kim, W. Bleck, Grain boundary strengthening in high Mn austenitic steels, *Metall. Mater. Trans. A* 47 (2016) 1918–1921.
 - [60] V. Turlo, T.J. Rupert, Grain boundary complexions and the strength of nanocrystalline metals: dislocation emission and propagation, *Acta Mater.* 151 (2018) 100–111.
 - [61] D. Clark, T. Russell, D. Wood, The influence of grain size on the yield phenomenon in steel, *Acta Metall.* 9 (1961) 1054–1063.
 - [62] N. Tsuchida, Y. Tomota, K. Nagai, K. Fukaura, A simple relationship between Lüders elongation and work-hardening rate at lower yield stress, *Scr. Mater.* 54 (2006) 57–60.
 - [63] D. Lloyd, L. Morris, Lüders band deformation in a fine grained aluminium alloy, *Acta Metall.* 25 (1977) 857–861.
 - [64] J. Butler, Lüders front propagation in low carbon steels, *J. Mech. Phys. Solids* 10 (1962) 313–318.
 - [65] B. Sun, R. Ding, N. Brodusch, H. Chen, B. Guo, F. Fazeli, D. Ponge, R. Gauvin, S. Yue, Improving the ductility of ultrahigh-strength medium Mn steels via introducing pre-existed austenite acting as a “reservoir” for Mn atoms, *Mater. Sci. Eng., A* 749 (2019) 235–240.
 - [66] R.H. Leal, J.R.C. Guimarães, Microstructure evolution during mechanically induced martensitic transformation in Fe-33%Ni-0.1%C, *Mater. Sci. Eng.* 48 (1981) 249–254.
 - [67] B. Rao, M. Rashid, Direct observations of deformation-induced retained austenite transformation in a vanadium-containing dual-phase steel, *Metallography* 16 (1983) 19–37.